Journal of Aerosol Science 174 (2023) 106235

Contents lists available at ScienceDirect

Journal of Aerosol Science

journal homepage: www.elsevier.com/locate/jaerosci

Characterization of a multi-stage focusing nozzle for collection of spot samples for aerosol chemical analysis☆

Orthodoxia Zervaki [a,b], Dionysios D. Dionysiou [b], Pramod Kulkarni [a,*]

[a] Centers for Disease Control and Prevention, National Institute for Occupational Safety and Health, Cincinnati, OH, 45226, United States
[b] Environmental Engineering and Science Program, Department of Chemical and Environmental Engineering (ChEE), University of Cincinnati, Cincinnati, OH, 45221, United States

ARTICLE INFO

Handling Editor: Chris Hogan

Keywords:
Aerodynamic focusing
Multi-stage
Converging nozzle
Impaction
Optical spectroscopy
Sensitivity
Portable instrumentation

ABSTRACT

Concentrated collection of aerosol particles on a substrate is essential for their chemical analysis using various microscopy and laser spectroscopic techniques. An impaction-based aerosol concentration system was developed for focused collection of particles using a multi-stage nozzle that consists of a succession of multiple smooth converging stages. Converging sections of the nozzle were designed to focus and concentrate a particle diameter range of 900–2500 nm into a relatively narrower particle beam to obtain particulate deposits with spot diameters of 0.5–1.56 mm. A slightly diverging section before the last contractions was included to allow for better focusing of particles at the lower end of the collectable diameter range. The characterization of this multi-stage nozzle and the impaction-based aerosol concentration system was accomplished both numerically and experimentally. The numerical and experimental trends in collection efficiency and spot diameters agreed well qualitatively; however, the quantitative agreement between numerical and experimental results for wall losses was poor, particularly for larger particle diameters. The resulting concentrated particulate deposit, a spot sample, was analysed using Raman spectroscopy to probe the effect of spot size on analytical sensitivity of measurement. The method's sensitivity was compared against other conventional techniques, such as filtration and aerosol focused impaction, implementing condensational growth. Impaction encompassing the multi-stage focusing nozzle is the only method that can ensure high sensitivity at Reynolds numbers greater than 2000, that can be supported by small pumps which renders such method suitable for portable instrumentation.

1. Introduction

Measurement of aerosol chemical components is essential for understanding the impact of aerosol exposure on human health (Davidson et al., 2005; Maynard & Kuempel, 2005; West et al., 2016). Long-term exposure to airborne particulate matter such as $PM_{2.5}$, ultrafine aerosols, or nanoparticles has been linked with dramatic impacts on human health. Particularly, cardiovascular diseases (Nemmar et al., 2002), pulmonary and systemic diseases and inflammation (Dockery & Pope, 1994; Oberdörster, 2001; C. Arden Pope

☆ Disclaimer – The findings and conclusions in this report are those of the authors and do not necessarily represent the official position of the National Institute for Occupational Safety and Health, Centers for Disease Control and Prevention.

* Corresponding author.
E-mail address: PSKulkarni@cdc.gov (P. Kulkarni).

https://doi.org/10.1016/j.jaerosci.2023.106235
Received 19 May 2023; Received in revised form 7 July 2023; Accepted 10 July 2023
Available online 14 July 2023
0021-8502/Published by Elsevier Ltd.

et al., 2004; Hoek et al., 2013) have been attributed to the inhalation of fine particulate matter, such as diesel particulate matter (DPM; Dowling, 2004) or asbestos and silica (Mossman & Churg, 1998). Measurement of airborne concentration and chemical composition of particulate contaminants is of critical importance to understand human exposure and the associated health effects.

Aerosol collection for subsequent analysis using laser spectroscopies, such as Raman spectroscopy, laser-induced breakdown spectroscopy, and spark emission spectroscopy, is a promising approach to obtain either near-real time or on-site detection of particulate matter (Diwakar et al., 2012; Diwakar & Kulkarni, 2012; Zheng et al., 2016, 2017; Wei et al., 2022). For these applications, the collection of airborne particulate matter as a 'spot sample', i.e. a particulate deposit with a diameter of about 1 mm or less, is essential to improve the method's sensitivity (Zervaki et al., 2023).

Murphy and Sears (1964) introduced the collimation of airborne particles into a narrow aerosol beam by using a high vacuum chamber encompassing axisymmetric capillaries to enhance the focusing of a range of aerodynamic sizes. Additionally, a converging nozzle was utilized for the generation of a narrow aerosol beam followed by impaction, indicating the ability of size segregation based on the particle size-dependent beam divergence (Dahneke & Flachsbart, 1972). Design and characteristics of conventional impactors based on inertia, encompassing focusing nozzles, have also been reported. Marple and Liu (1974) were among the first to examine the impact of the distance between the collection plate and the nozzle, the Reynolds number at the exit of the nozzle and the nozzle throat length on the impactor's collection efficiency. Aerosol beam collimation can be similarly achieved by using aerodynamic lenses, a sequence of co-axial contractions and expansions, for nudging the airborne particles closer to the central axis (Liu et al., 1995a; Liu et al., 1995b). Narrow aerosol focusing is also attained when a rapidly converging nozzle is used, providing a beam divergence considerably smaller than the nozzle diameter, leading to high concentration of particles along the central axis (Fernández de la Mora & Rosell-Llompart, 1989; Rao et al., 1993). Virtual impaction has also been used to concentrate high inertia-particles along the central axis (Barr et al., 1983; Sioutas, Koutrakis, & Burton, 1994). Due to this method's efficiency at separating coarse from fine particles, virtual impactors have been used as pre-selective size inlets for optical particle counters (Lehtimäki and Janka 1987) and for toxicological studies (Demokritou et al., 2002). However, this collection method suffers from the lack of "sharpness" of the transmission efficiency curve (Sioutas, Koutrakis, & Olson, 1994) and the inability to generate a tight collimated aerosol beam. Moreover, most of these techniques require bulky vacuum pumps, hence they are not appropriate for handheld or field portable instrumentation.

In this study, a new approach is presented that uses a series of slowly converging sections that allows particle beam formation and spot collection via impaction at relatively high flow rates.

2. Design of multi-stage focusing nozzle

A multi-stage focusing nozzle (MSN) with curvilinear converging walls was designed, fabricated, and tested. The design is adopted from a similar nozzle proposed for laminar, high flow rate flows by Vidal-de-Miguel and de la Mora (2012). They proposed slowly converging sections with smooth walls to allow laminar flow at high Reynolds number (>2000) to aid particle focusing. We used similar converging and diverging sections in our design, and we present both the numerical simulation and experimental evaluation of the MSN and a one-stage focusing nozzle (OSN) used as a reference, in the flowrate range of 0.4–2 L min^{-1}.

Several designs consisting of varying cross-sectional wall curvature, the rate of convergence (as measured by the change in diameter of the opening along the axis), and number of converging and diverging sections, were numerically tested to optimize the penetration efficiency through the nozzle, the collection efficiency on the deposition surface as a function of particle size, the diameter of the spot deposit formed, and the aerosol sampling flow rate. The key consideration was that a series of contractions should successively concentrate a broad range of particle sizes into a tighter aerosol beam. The first few converging sections allow for focusing of larger particles, while the subsequent sections can focus smaller particles along the centreline axis, while not allowing defocusing of previously focused larger particles. Moreover, a section with a slight divergence prior to the last converging stages was added to achieve better focusing of small particles closer to the central axis.

The Stokes number for this nozzle is defined by Hinds (1999) as the ratio of the particle's stopping distance to the nozzle radius,

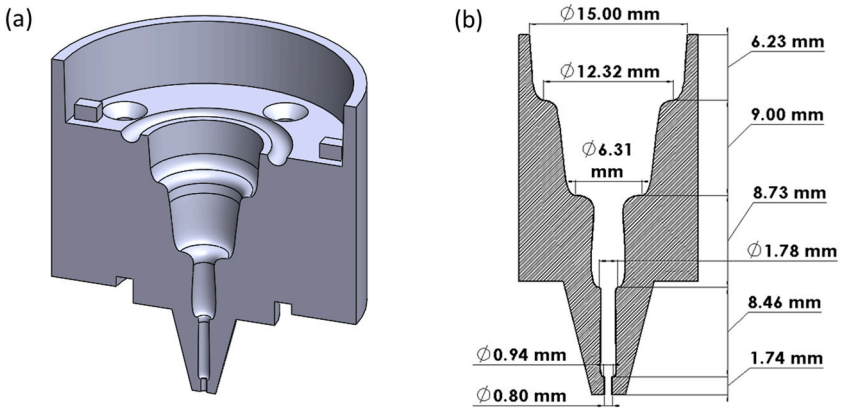

Fig. 1. (a) 3D cross sectional view and (b) 2D cross sectional view with dimensions of the multi-stage converging nozzle.

given as:

$$Stk = \frac{\rho_p {d_p}^2 U C_c}{9\mu D_j} \tag{1}$$

where ρ_p is the particle density, d_p is the particle diameter, U is the air velocity, C_c is the Cunningham slip correction factor, μ is the air dynamic viscosity and D_j is the nozzle diameter. The square root of Stokes number ($\sqrt{Stk}$) was used to assess performance of the nozzle as it represents dimensionless particle size.

Fig. 1(a) illustrates the multi-stage focusing nozzle (MSN) design that represents an optimum trade-off between penetration efficiency, collection efficiency, and particle beam or spot size. The particle-laden stream enters the focusing nozzle through a cyclic surface with a diameter equal to 15 mm. Then, gradual convergence of the aerosol beam is attained by a series of contraction stages succeeding the nozzle inlet. Right before the last two contraction stages, a slight divergence, as it was noted through numerical simulations, acted as a "slide" for the finer particles, allowing better focusing closer to the central axis. The orifice diameter where particles form a narrow-focused beam and exit the nozzle, is 0.8 mm. The length of the multi-stage converging nozzle is 34 mm. The dimensions of each individual stage included in the nozzle are presented in Fig. 1(b).

3. Numerical simulations

A numerical model was developed to simulate fluid flow and the resulting particle trajectories using a finite element method (Comsol™ Multiphysics; v 5.4). A 2D axisymmetric laminar model was used to solve the following Navier-Stokes equations along with the continuity equations:

$$\rho\left(\frac{\partial u}{\partial t} + u\nabla u\right) = -\nabla p + \mu\nabla^2 u + \frac{1}{3}\mu\nabla(\nabla u) + \rho g \tag{2}$$

$$\nabla(\rho u) = 0 \tag{3}$$

where, ρ is the air density, u is the air velocity vector, p is the pressure, μ is the fluid dynamic viscosity, g is the gravitational acceleration constant, and t is the time.

Additionally, the turbulent flow model was also developed to investigate the nozzle performance if the flow were to become turbulent at high flow rates. The specific v2-f module was selected due to its suitability for enclosed flow over curved surfaces. The equations used for the turbulent v2-f flow module are presented in detail in Section S1 in SI.

For the numerical computation, the flow was assumed to be compressible and at steady state at 20 °C. A pressure boundary condition was assigned at the inlet, equal to 101.3 kPa. A volumetric flow boundary condition with a flow rate of 2 L min^{-1} was assigned downstream of the collection substrate. A no-slip boundary condition was applied at the walls. The constructed mesh was adapted to the physics settings within the model and consisted of free triangular elements with an extremely fine or extra fine density across the nozzle. A convergent solution could be obtained for the flow field with a minimum of 33,600 mesh elements. To obtain particle trajectory, the built-in Particle Tracing module in COMSOL was used along with a time-dependent study. To ensure accurate prediction of the particle trajectories, a simulation was conducted using 55,049 mesh elements. The numerical results for wall losses, spot deposit and collection efficiency were found to be unaffected by the number of mesh elements used. Therefore, a total of 33,600 mesh elements were selected for convenience in terms of storage space and time requirements. Since the aerosol was a dilute suspension with a low volume fraction, the assumption that the particles' motion was affected by the fluid flow but not vice-versa, was justified. Once the fluid velocity profiles were obtained, the particle trajectories were calculated using the flow field, and were governed by the following equations:

$$v = \frac{dq}{dt} \tag{4}$$

$$\sum F = m_p \frac{dv}{dt} \tag{5}$$

where q is the particle's position, v is the velocity of the particle , m_p is the mass of the particle and $\sum F$ is the sum of forces acting on the particle. Equations (4) and (5) were used for the calculation of the particle's position and velocity, respectively. Following forces acting on the particle were considered (Clift et al., 1978; Li & Ahmadi, 1992; Kim & Zydney, 2004):

$$F_D = \frac{1}{\tau_p S} m_p (v - v_{fluid}) \quad \text{where} \quad \tau_p = \frac{\rho_p {d_p}^2}{18\,\mu} \tag{6}$$

$$S = 1 + \frac{\Lambda}{d_p}\left(C_1 + C_2\, exp\left(-\frac{C_3 d_p}{\Lambda}\right)\right) \tag{7}$$

$$F_B = \zeta\sqrt{\frac{6\,\pi k_b \mu T d_p}{\Delta t}} \tag{8}$$

where F_D is the drag force acting on the particles, v_{fluid} is the velocity of the fluid, τ_p is the particle velocity response time, S is the slip correction factor, ρ_p is the particle density, d_p is the particle diameter, Λ is the mean free path, C_1, C_2 and C_3 are the parameters in the Cunningham-Millikan-Davies slip correction factor equation (Equation (7)), with assigned default values of 2.514, 0.8 and 0.55, respectively (Allen & Raabe, 1982; Davies, 1945), F_B is the Brownian force, ζ is a dimensionless vector of normally distributed random numbers with zero mean and unit standard deviation, k_b is the Boltzmann's constant, T is the absolute fluid temperature, and Δt is the time step taken by the numerical solver. The drag force acted on all particles (Equation (6)) due to the laminar or turbulent fluid flow, while the Brownian force (Equation (8)) was applied to particles with a diameter less than 500 nm. Gravitational force was assumed to be negligible for the particle diameters considered in this study. As an initial condition, the particle velocity was set to be equal to the fluid velocity. The particles were assumed to be spheres with a density of 1 g cm^{-3}. A total number of a 100 monodisperse particles, uniformly distributed, were released simultaneously at the inlet boundary. A time step of 10^{-5} s was used to obtain adequately space- and time-resolved particle trajectories. Simulations using smaller time steps did not affect the numerical results. The default generalized alpha numerical algorithm was employed for the particle trajectory calculations. Particles were assumed to "freeze" after depositing on the nozzle walls, while "particle bouncing" was selected as a wall condition for the axisymmetric axis.

The transmission efficiency through the MSN and the OSN for a wide range of particle diameters was obtained using the numerical model calculations as the fraction of the number of particles that reached the nozzle outlet to the total number of particles that were released at the nozzle inlet. Similarly, the collection efficiency of the particles concentrated on the collection plate was computed. The deposition area diameter, where 90% of the particles were deposited, or the spot diameter was also calculated.

4. Experimental methods

The MSN was 3D printed using plastic material of high clarity and resolution via Stereolithography (3DSystems, Rock Hill, SC, USA), which provided high precision and accuracy, with a tolerance of less than 0.05 mm. The printing was produced by a 3D model constructed in Solidworks (Dassault Systemes). A transparent, polycarbonate-like, plastic material was selected (Accura ClearVue; 3DSystems, Rock Hill, SC, USA), for detailed and smooth surface finish. We have designed and tested a reference one-stage focusing nozzle (OSN) that had the same axial length, inlet, and outlet diameters, and was used for comparing the performance of the multi-stage nozzle. The OSN was fabricated through the PolyJet™ 3D printing process (Stratasys Objet Eden 260 VS; Stratasys, Eden Prairie, MN, USA), providing an accuracy in the range of 25–80 μm, in a transparent, photopolymer material (VeroClear™ RGD810™; Stratasys, Eden Prairie, MN, USA) for enhanced surface smoothness.

Several collection surface designs with varying geometry were tested numerically. Curvy impaction substrates were previously found to improve collection efficiency, decreasing significantly the cut-off size of the collection efficiency curve (Kim et al., 2013). However, narrow distribution of finer particles collected could not be attained employing this design numerically. For the current study, a flat plate was used as a collection substrate, where the particles were impinged on. The collection plate was made of tungsten and had a width of 1.56 mm and a length of 6 mm. The optimized distance between the jet and the collection plate selected, was 1.5 mm.

The experimental set up used for the MSN characterization is presented in Fig. S-1 in SI. Liquid solutions of ammonium sulfate were aerosolized by a medical nebulizer (Salter 8900 Series Disposable Small Volume Jet Nebulizer; Salter Labs, Arvin, CA, USA). The generated aerosol stream was dried by a diffusion dryer and then the polydisperse aerosol sample passed through the Aerodynamic Aerosol Classifier (AAC; Cambustion Ltd, Cambridge, United Kingdom) which produced monodisperse aerosol streams. Excess of air flow was removed by a vacuum pump. The air flow rate through the AAC was controlled at approximately 0.4 L min^{-1}. A humidifier (MH-110-12F-4; Perma Pure LLC, NJ, USA) was located prior to the impactor encompassing the focusing nozzle, for eliminating particle bouncing on the collection surface. An Ultrafine Condensation Particle Counter (model UCPC 3776, TSI Inc., Shoreview, MN, USA) was employed for calculating the wall losses at the interior of the focusing nozzle and the collection efficiency of the impaction-based micro-concentrator.

The wall losses in the interior of the nozzle were measured as shown in Fig. S-1(a). The fraction of the number of particles trapped in the nozzle was estimated using the following equation:

$$\eta_{loss} = \frac{N_{in} - N_{out}}{N_{in}} \tag{9}$$

where η_{loss} denotes the losses, N_{in} (cm^{-3}) is the number concentration of particles measured upstream of the nozzle and N_{out} (cm^{-3}) is the number concentration of particles measured downstream of the nozzle.

The collection efficiency curves for the MSN and the OSN were experimentally measured using an impactor encompassing the focusing nozzle and a collection plate located 1.5 mm away from the nozzle jet (Fig. S-1(b)). The collection efficiency (η_c) was calculated as follows:

$$\eta_c = \frac{N_{w/o\ imp} - N_{w/\ imp}}{N_{w/o\ imp}} \tag{10}$$

where $N_{w/o\ imp}$ (cm^{-3}) is the number concentration of particles measured at the absence of the collection plate and $N_{w/\ imp}$ (cm^{-3}) is the number concentration of particles counted when the collection plate was located downstream of the nozzle jet.

The flow was regulated downstream of the nozzle or the impactor by the pump contained in the UCPC at approximately 1.5 L min^{-1}, along with an additional vacuum pump which was used for maintaining the air flow rate at the nozzle/impactor inlet at

approximately 2 L min^{-1}.

The particulate sample accumulated on the collection flat plate, i.e. the 'spot sample', was analysed using Raman Spectroscopy. During the sample collection the UCPC was connected at the inlet of the impactor, monitoring the number of particles entering the focusing nozzle, while a pump regulated the flow through the impactor at 2 L min^{-1}. The nominal analyte mass, based on the inlet aerosol concentration upstream of the impactor, was then calculated:

$$m_p = Q\, t_c\, N_{in}\, \rho_p\, V_p \tag{11}$$

where Q is the sample flowrate (L min^{-1}), t_c is the sample collection time (min), N_{in} is the measured particle number concentration upstream of the nozzle (cm^{-3}), ρ_p is the density of ammonium sulfate (1.77 g cm^{-3}) and V_p is the volume of the particles, assuming spherical shape. Ammonium sulfate particles of different aerodynamic diameters (d_p= 1000, 1500, 2000 and 2500 nm) were concentrated on the collection substrate and different calibration curves for each particle diameter were extracted. A portable Raman spectrometer was used for the analysis (i-Raman®; B&W Tek, Newark, DE, USA). The excitation wavelength used in the spectrometer was 785 nm, with 420 mW of power. The working distance was approximately 9 mm, and the diameter of the laser beam was approximately 105 μm. The integration time selected for the spectra acquisition was 30 s. For the ammonium sulfate particles used for the characterization, the peak signal intensity is observed at a Raman shift of approximately 977 cm^{-1}. Three replicates were obtained for each measurement by acquiring spectra from three different spots of the deposited sample. The average areas of the peaks were estimated for the extraction of calibration curves providing the association between the Raman signal intensity and the particulate mass accumulated on the collection plate.

5. Results and discussion

5.1. Particle trajectories and spot deposition characteristics from numerical simulations

The flow velocity profile, particle trajectories for different particle sizes, and the deposition spot diameter on the collection plate were numerically simulated. The performance of the MSN was evaluated and compared with the OSN. The velocity profile obtained from the laminar flow model is shown in Fig. 2. The wall located at 1.5 mm downstream of the nozzle opening represents the collection plate.

In the MSN, a low velocity gradient was observed, particularly before the last converging stage, when the laminar flow module was implemented (Fig. 2(a)). On the other hand, in the OSN the velocity gradient is much higher right before the nozzle exit. In both nozzles the highest velocity values are observed closer to the central axis, approximately in the range of 75–80 m s^{-1}. That velocity range corresponds to Re greater than 4000 which commonly indicates turbulent flow. However, Vidal de Miguel and de la Mora (2012) have shown that laminar flow can be maintained at high Reynolds number for such gradually converging contractions. We conducted numerical simulations of the OSN and MSN using a turbulent flow model, which showed similar flow field distribution as in the case of laminar flow model (Fig. S-2 in SI).

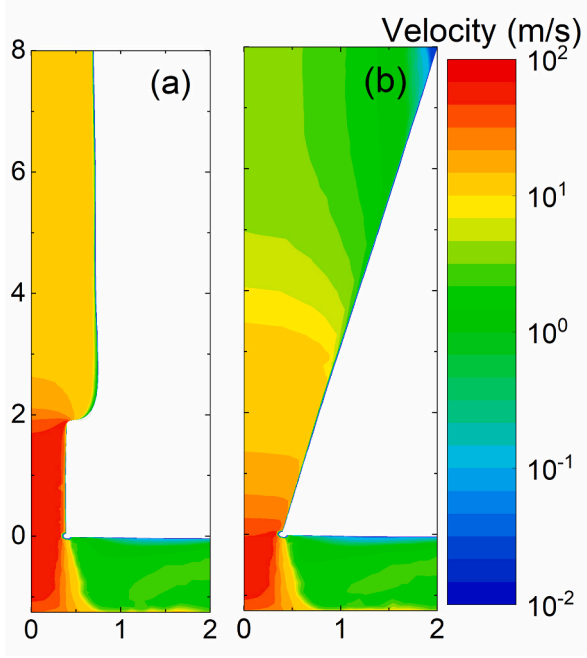

Fig. 2. Velocity profile (m s^{-1}) derived by numerical simulations of laminar flow at 2 L min^{-1} for the (a) multi-stage and the (b) one-stage focusing nozzle. X- and Y- axis show distances in units of millimeters.

The trajectories of particles with diameters of 500, 1000 and 2500 nm in MSN and OSN are shown in Fig. 3. Better focusing of the particle beam in MSN is clearly evident. Prior to the last contraction, better focusing is rendered for larger particles (d_p= 2500 nm). After the latter converging stage, the particle beam is more concentrated closer to the central axis until it finally impinges on the collection plate. On the other hand, in the OSN the focusing is not as efficient (Fig. 3(b)). However, for both MSN and OSN the beam width formed for particles with a diameter of 500 nm is larger than the collection substrate.

Fig. 4 shows spot diameter obtained from simulations for various particle diameters for both OSN and MSN. The spot diameter is inversely proportional to the particle size. The MSN focuses the particles into relatively well-defined circular beams (Fig. 4(a)) whereas OSN spot samples are relatively smeared (Fig. 4(b)). Fig. S-3 in SI shows radial distribution of particle position within each spot shown in Fig. 4, which clearly shows better focusing ability of the MSN.

5.2. Experimental and numerical wall losses and penetration efficiency

The loss of particles to the nozzle wall are shown in Fig. S-4(a) and (b) in SI. The wall losses (η_{loss}) were determined both numerically and experimentally.

Quantitative agreement between experimental and numerical values is poor, particularly for higher $\sqrt{Stk}$. The experimental particle losses were found to be approximately 1%–8% for particles in the $\sqrt{Stk}$ range of 0.26–1.27 (d_p=300–1700 nm) for the MSN (Fig. S-4(a) in SI), while they rapidly increase beyond approximately 50% for $\sqrt{Stk}$ equal to 1.84 (d_p=2500 nm). The numerical simulations (for both laminar and turbulent cases) indicated that wall losses appear mainly on the last two converging stages, for $\sqrt{Stk}$ greater than 2.20 (d_p=3000 nm) and reach approximately the value of 50% at 9.34 (d_p=13000 nm).

When the OSN is used, losses found experimentally were approximately 0%–11% for $\sqrt{Stk}$ smaller or equal to 0.62 (d_p=800 nm), while they reach the value of 46% for $\sqrt{Stk}$ equal to 1.84 (d_p=2500 nm). No wall losses are numerically predicted for $\sqrt{Stk}$ smaller or equal to 6.84 (d_p=9500 nm), while a 50% cut point at 8.62 (d_p=12000 nm) was calculated through the laminar flow module. No losses are predicted for $\sqrt{Stk}$ up to at least 10.77 (d_p=15000 nm), using the turbulent module.

Numerical simulations conducted for various geometries showed that the transmission efficiency was only dependent on the exit nozzle diameter rather than the specific geometrical configuration of the nozzle. This is consistent for both the MSN and the OSN. The experimental wall losses were observed to be inversely proportional to the nozzle diameter (Fig. S-5 in SI). Wall losses were negligible when the nozzle diameter was greater than 1.6 mm which corresponds to the Reynolds number of <1770. It is not clear if the surface roughness of the inside wall of the nozzle, originating from imperfections introduced during 3D printing, could lead to onset of local turbulence, and explain the disagreement between experimental and numerical results. To further probe if the loss is correlated with the Re number, particle loss was examined at lower aerosol flow rate of 0.4 L min^{-1} (Re=700) (Fig. S-6 in SI). The numerical results showed no significant wall losses, (0–4%), for $\sqrt{Stk}$ in the range of 0–1. Experimental results also agreed with this trend, showing negligible losses for $\sqrt{Stk}$ <0.8, and about 20% losses for $\sqrt{Stk}$ ≥0.8. Increased losses observed at higher flow rates could possibly be attributed to local flow distortion from imperfect internal surfaces at higher Re number. To further examine the reason for the losses, fluorescent monodisperse particles with a diameter of 3 μm, passed through the MSN. The particles were mainly deposited on the internal walls of the last two contractions, with diameters of 1.76 and 0.90 mm, respectively. It is possible that the 3D printed parts used in this study had suboptimal surface roughness which contributed to particle loss. To mitigate this, alternative materials and fabrication techniques could be explored. Electroplating process has been increasingly utilized to minimize surface roughness in various applications, and it could provide the desired surface smoothness of the nozzle interior surfaces (Fallah et al., 2021; Zhu et al., 2008). To further enhance the performance of the MSN, using an additional sheath flow that surrounds the axial aerosol flow, can be

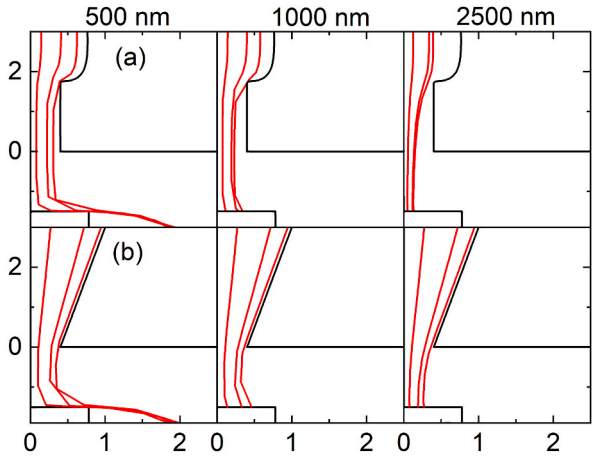

Fig. 3. Numerical simulation of particle trajectories with different diameters (500, 1000 and 2500 nm) for (a) the multi-stage focusing nozzle and (b) the one-stage focusing nozzle, for a flow rate of 2 L min^{-1}. The X- and Y- axis represent distances in units of millimeters. The exit of the nozzle is located at Y=0, and the collection plate is located at Y= −0.0015.

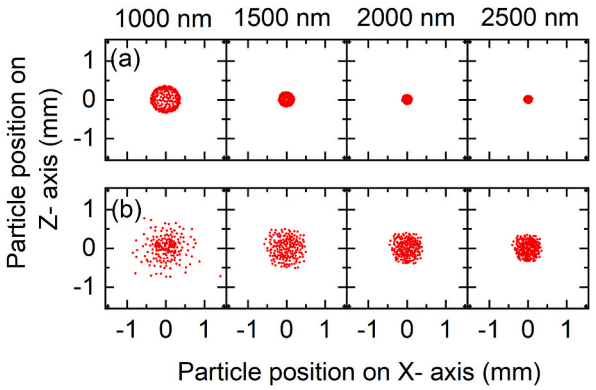

Fig. 4. Numerical simulation's distribution of particles with aerodynamic diameters of 1000, 1500, 2000 and 2500 nm on the collection plate for a flow rate of 2 L min^{-1} for (a) multi-stage focusing nozzle and (b) one-stage focusing nozzle.

explored. The sheath flow, much higher than the aerosol flow rate, can shield the aerosol flow from wall imperfections, thereby reducing the particle loss and improving the spot diameter.

Fig. 5 shows the overall penetration efficiency as a function of particle diameter for both MSN and OSN measured experimentally; also shown for comparison is the $PM_{2.5}$ fraction curve (Hinds, 1999). The penetration efficiency curve of the MSN appears to approximate the $PM_{2.5}$ fraction well and therefore, it can be used as a $PM_{2.5}$-selective inlet. Moreover, the penetration efficiency curve of the MSN is sharper than the corresponding efficiency curve provided by the OSN (Section S2 in SI).

5.3. Impaction collection efficiency

The collection efficiency curves are shown in Fig. 6. During the particle collection, the high impaction velocity of the particles exiting the nozzle outlet, can render reduced collection efficiency resulting from losses from particle bounce. To probe if the particle bounce was significant, the collection efficiency was also measured with the thin coating of silicone vacuum grease (Beckman Instruments Inc., Palo Alto, Ca), which significantly reduces bounce. Measured collection efficiencies in Fig. 6, with and without coating of grease, indicate absence of significant particle bounce.

Good agreement was observed between the qualitative trends in experimental and numerical results. Collection efficiency curves obtained numerically indicated a collection efficiency of 50% at $\sqrt{Stk_{50}}$ of 0.49 for the MSN and 0.51–0.52 (for the laminar and the turbulent module) for the OSN. Experimentally, a small deviation was observed, while the $\sqrt{Stk_{50}}$ is approximately 0.69 for both nozzles, corresponding to a particle diameter of 900 nm. The sharpness of the collection efficiency curve obtained experimentally for

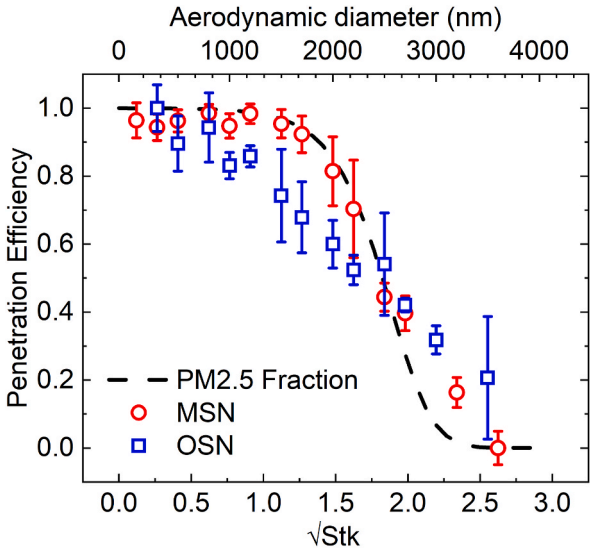

Fig. 5. Penetration efficiency curve at 2 L min^{-1} as a function of the square root of the Stokes number (and the aerodynamic diameter), for the multi-stage and the one-stage focusing nozzle along with the $PM_{2.5}$ penetration curve. The error bars indicate the standard deviation that was calculated from the three replicates.

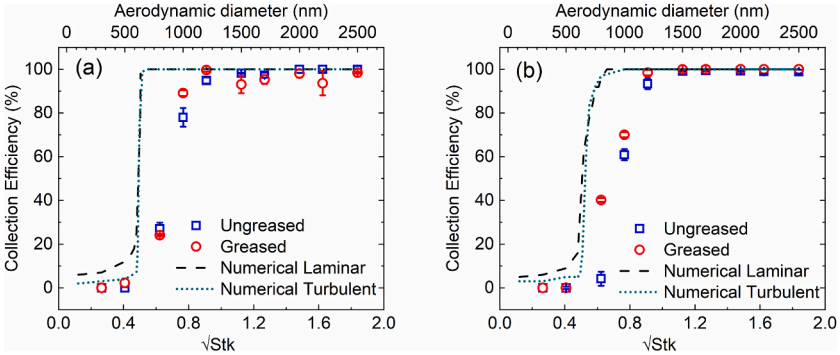

Fig. 6. Experimental and numerical collection efficiency curves at 2 L min^{-1} as a function of the square root of the Stokes number (and the aerodynamic diameter) for (a) the multi-stage nozzle and (b) the one-stage nozzle. The error bars indicate the standard deviation that was calculated from the three replicates.

the MSN and the OSN was 1.3 and 1.16 respectively. Good agreement with the simulation was shown when both the uncoated and the coated flat collection plate was used. This was attributed to the humidification of the aerosols prior entrance to the nozzle, minimizing the particle bouncing.

5.4. Total collection efficiency

The particle size-dependent total efficiency of the MSN, which is the product of nozzle's penetration efficiency and the impactor collection efficiency, is shown in Fig. S-7 in SI. Experimental data show that the MSN embodied in the impactor can collect particles in the $\sqrt{Stk_{50}}$ range of 0.69 and 1.84, approximately. The best fits to the size-dependent efficiency curves (η) could be described using the following equations:

$$\eta = 0.01062 - \left(0.46319\sqrt{Stk}\right) + \left(1.06589\sqrt{Stk}^2\right), \sqrt{Stk} \le 0.91 \tag{12}$$

$$\eta = -0.37544 + \left(2.20225\sqrt{Stk}\right) - \left(1.09722\sqrt{Stk}^2\right) + \left(0.1432\sqrt{Stk}^3\right), \sqrt{Stk} > 0.91 \tag{13}$$

Using Equations (12) and (13), calculations were performed to obtain the total particulate mass collected on the impaction substrate for a given particle size distribution entering the nozzle inlet. The percent bias between the mass collected on the impactor containing the MSN ($M_{impactor}$) and the corresponding mass collected on $PM_{2.5}$ Samplers ($M_{PM2.5}$; Hinds, 1999) can be calculated:

$$Bias\ (\%) = 100\frac{M_{impactor} - M_{PM2.5}}{M_{PM2.5}} \tag{14}$$

Particle volume and mass were calculated using spherical shape and density of 1 g cm^{-3}. Lognormal number distributions with different geometric means (d_g) and geometric standard deviations (σ_g) were used for the extraction of the total number of particles collected in the impactor with the MSN and on $PM_{2.5}$ samplers. A total of hundred particles were assumed and the calculation of the fraction of particles (df) as a function of the natural logarithm of the particle diameter (d_p) was obtained:

$$df = \frac{1}{\sqrt{2\pi}\ ln\ \sigma_g}\exp\left(-\frac{\left(\ln d_p - ln\ CMD\right)^2}{2\left(ln\ \sigma_g\right)^2}\right) d\ln d_p \tag{15}$$

For a lognormal number distribution, the Count Median Diameter (CMD) is equivalent to the geometric mean diameter, d_g (Hinds, 1999).

Fig. 7 illustrates the percent bias distribution, as a function of geometric mean diameter and the geometric standard deviation of an aerosol size distribution of the aerosol entering the MSN. Fig. 7 shows that the bias is less than 25% when the aerosol has the geometric mean and standard deviation in the range of approximately 1–2.5 μm and 1.0 to 3.0, respectively.

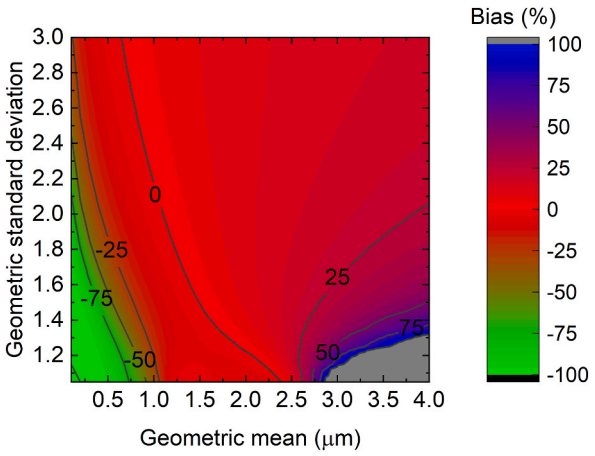

Fig. 7. Percent bias of the total mass collected through impaction using the multi-stage converging nozzle compared to a $PM_{2.5}$ sampler, as a function of the geometric mean and the geometric standard deviation of an aerosol lognormal number distribution.

5.5. Spot sample characteristics

Fig. 8 shows variation of spot sample diameter as a function of $\sqrt{Stk}$ obtained numerically as well as experimentally for MSN and OSN. The spot diameter is inversely proportional to the particle diameter, as predicted by the numerical simulation (Fig. 4). The focal point of larger particles is smaller, resulting in smaller deposition spots, compared to that for the finer particles (Sethi & John, 1993). The experimental spot diameter was roughly estimated from the images shown in Fig. S-8 in SI. Specifically, for aerodynamic diameters ranging from 1000 to 2500 nm ($\sqrt{Stk_{50}} = 0.8–1.8$) we obtained spot deposit diameters of 1.3 to 0.6 mm for MSN (Fig. 8(a)) and 1.4 to 0.8 mm for the OSN (Fig. 8(b)). Moreover, different patterns were observed on the accumulated deposition spots depending on the particle diameter (Fig. S-8 in SI). Burwash et al. (2006) noted different ring-shaped deposition patterns depending on the ratio of the nozzle-to-plate distance to the nozzle diameter for a given particle diameter. Additionally, Fredericks and Saylor (2018) reported inversely proportional relation of the particle diameter and the inner diameter of the ring-shaped deposition pattern. Generally, the focal point of the particle beam is regulated by the Stokes number.

Smaller deposition areas are predicted by the numerical simulations. For aerodynamic diameters ranging from 1000 to 2500 nm ($\sqrt{Stk_{50}} = 0.8–1.8$) the MSN is estimated to have spot deposit diameters of 0.65 to 0.25 mm (Fig. 8(a)) while the OSN is predicted to have spot deposit diameters of 1.0 to 0.6 mm (Fig. 8(b)). These estimates are based on the numerical results (D_{90}; spot deposit diameter where 90% of the collected particles are located) obtained from the simulation conducted a priori. Nevertheless, critical improvement is shown when the MSN is used compared to OSN. The deposition spot widths were distinctively smaller than those obtained from the OSN, as expected according to the numerical simulation's results presented in Fig. 4. Particularly, when 800 nm-diameter particles were used, better focusing was observed for the MSN in contrast to the OSN that showed a poor collection performance. This was also depicted in the collection efficiencies measured experimentally (approximately 27% and 4% for the MSN and the OSN, respectively, as presented in Fig. 6).

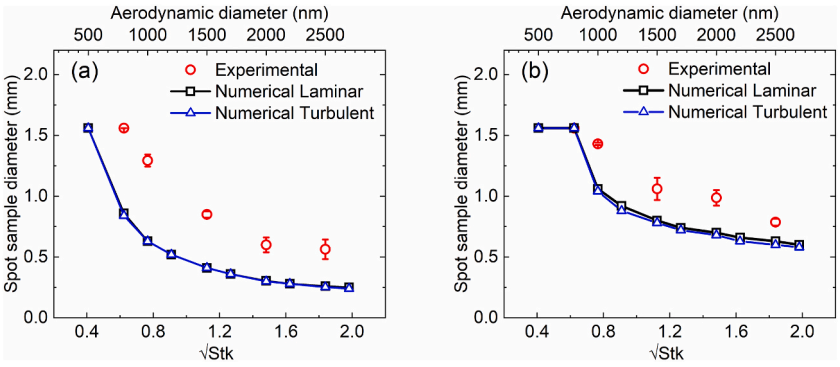

Fig. 8. Diameter of spot sample obtained numerically (D_{90}) and experimentally for (a) the multi-stage focusing nozzle (MSN) and (b) the one-stage focusing nozzle (OSN).

5.6. Improvement in analytical sensitivity of Raman spectroscopy analysis

The collected particulate mass on the flat surface was analysed by Raman spectroscopy to probe improvement in sensitivity of MSN compared to that of OSN and other particle collection techniques. Calibration curves of the signal intensity were extracted as a function of the ratio of the particulate mass accumulated on the collection plate per unit of deposition area– herein called surface mass density (Fig. 9):

$$I = S^* \frac{m_p}{A} \tag{16}$$

where the signal intensity by Raman spectroscopy is denoted by I, S^* is the slope of the line that represents the linear fitting to the experimental data with a fixed intercept to zero, m_p is the particulate mass collected on the plate (ng) and A is the deposition area of the collected spot (mm^2). Classified aerosol particles of $(NH_4)_2SO_4$ of different aerodynamic diameters (1000 nm, 1500 nm, 2000 nm and 2500 nm) were used. The deposition area for each particle diameter was obtained by the numerical simulation. The slopes (S^*) and R^2 values of the linear curves fitted on the data acquired are shown in Tables S–1 in SI.

The Raman intensity is a function of the diameter of the collected particles (Schrader et al., 1991; Stacey et al., 2021). This effect is shown in Fig. 9, where an increase of the particle diameter contributes to an increase of the calibration's curve slope. Particle size dependent spectroscopic response can contribute to the overall uncertainty of analytical measurement. To reduce this uncertainty in real world applications, the MSN can be calibrated using a polydisperse reference aerosol that closely matches in size distribution to the ambient or workplace aerosol of interest.

In Fig. 9, each calibration's curve slope can serve as the indicator of the analytical measurement sensitivity for a specific aerodynamic diameter. The slopes were estimated in the range of 1.1–10.04 $mm^2\ ng^{-1}$ for $(NH_4)_2SO_4$ particles for an aerodynamic diameter range of 1000–2500 nm.

The intrinsic spectroscopic sensitivity calculated in the current study (S^*) is dependent on the analyte used, the particle size distribution and the spectroscopic method applied for the signal intensity acquisition, but not the collection method.

Aerosol collection methods such as conventional filtration and the Sequential Spot Sampler™ (Series 110, Aerosol Devices Inc., Fort Collins, CO, USA) were selected for the method sensitivity comparison. Using Equation (16) and that $m_p = \eta Q\, t_c\, C_{in}$, the signal intensity can be calculated:

$$I = \frac{S^* \eta\, Q\, t_c}{A}\, C_{in} \tag{17}$$

where η is the method's collection efficiency, and C_{in} is the concentration of the collected sample ($ng\ m^{-3}$). The method sensitivity (S_c) was then calculated:

$$S_c = \frac{S^* \eta\, Q\, t_c}{A} \tag{18}$$

Table 1 illustrates operating conditions and design parameters used for the calculation of the method sensitivity of the conventional collection techniques. These conditions and parameters include the collection efficiency, the sample flowrate, the diameter of the deposition area of the accumulated sample and the collection time for each technique. The efficiency of particulate sample collection

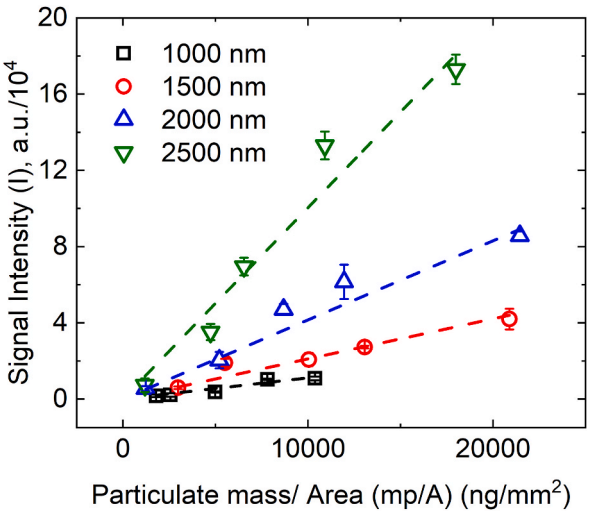

Fig. 9. Calibration curves for the particulate mass of $(NH_4)_2SO_4$ aerosol per unit of deposition area for different aerodynamic diameters. The dashed lines represent the linear fitting of the signal intensities of each aerosol diameter.

Table 1
Design and operating parameters for conventional aerosol collection methods used for method sensitivity comparison.

Collection method	Collection Efficiency	Sample Flow Rate (L min^{-1})	Diameter of deposition area (mm)	Collection time (min)
Impaction with MSN	0–0.94	2	0.24–1.56[a]	1
Filtration	1.0	2	25	1
Sequential Spot Sampler™	0.9–1.0	1.5	1.0	1

[a] The diameter of the deposition area was acquired numerically for the sensitivity comparison.

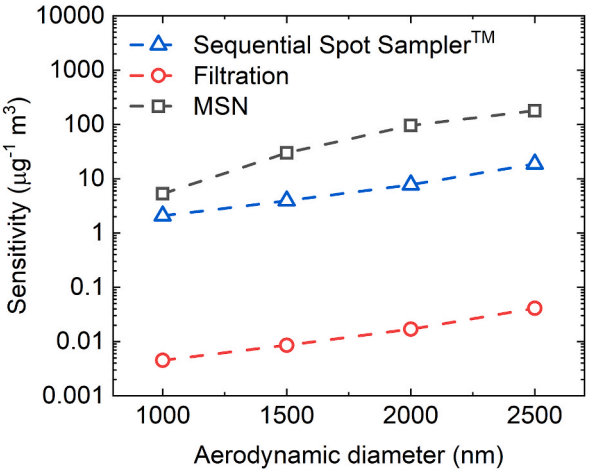

Fig. 10. Measurement sensitivity provided by impaction using the multi-stage focusing nozzle, compared to other focusing and collection methods, such as filtration, and the Spot Sampler™.

through filtration or the Sequential Spot Sampler™ is size-independent. Additionally, the spot deposit formed is assumed to be size-independent. In Fig. 10, the method sensitivity (S_c) is shown as a function of the aerosol aerodynamic diameter. Impaction using the MSN appears to provide approximately 3–4 magnitudes of order higher sensitivity than the conventional collection method using filtration. Additionally, higher sensitivity is observed against the Spot Sampler™ for an aerodynamic diameter range of 1000–2500 nm. Impaction encompassing the multi-stage focusing nozzle (MSN) is the only collection technique that can ensure high sensitivity– for particles >1000 nm– at high Reynolds numbers that can be supported by small pumps that makes it well-suited for portable instrumentation.

The calibration curves of the signal intensity extracted, regarding the mass accumulated on the collection plate, for the MSN and the OSN, are presented in Fig. S-10(a) in SI. Monodisperse aerosol sample of ammonium sulfate was generated with an aerodynamic diameter of 2500 nm. The "tighter" distribution on the collection plate resulted by the MSN yielded an upsurge in the method sensitivity approximately by a factor of four, compared to the focusing achieved by the OSN (S^*_{MSN}=189.2, S^*_{OSN}= 46.3). Moreover, the intensity of the spectroscopic signal collected when the sample was accumulated on a bigger surface than the original is presented in Fig. S-10(b) in SI. The slope of the calibration curve slightly improves, indicating that the sample has a narrower distribution on the wider collection surface and the sensitivity of the method can be improved.

6. Conclusions

An impaction-based aerosol spot sample collection scheme consisting of a gradually converging multi-stage nozzle was developed and characterized in this study. Improved transmission and collection efficiency is observed when the multi-stage nozzle is used, compared to the conventional one-stage nozzle. Using the multi-stage nozzle, smaller spot samples in the aerosol diameter range of 900 nm–2500 nm could be obtained. Larger particles resulted in smaller spot samples. The multi-stage converging nozzle provides a well-defined spot sample compared to the one-stage nozzle. Compared to the one-stage nozzle, the multi-stage nozzle provided a reduction of 10, 39 and 29% in spot diameter for particles with Stokes number of 0.8, 1.5, and 1.8 respectively. Qualitative trends from numerical simulations and experimental data agreed well; however, quantitative agreement was poor, particularly with respect to the magnitude of the wall losses. The difference could likely be explained by local flow perturbations induced by imperfections or wall roughness of the interior nozzle surfaces leading to greater particle loss. The spot samples sizes obtained were found to be adequate to provide enough sensitivity for Raman analysis for typical workplace aerosol concentrations. The spectroscopic sensitivity for the multi-stage nozzle, was higher by a factor of four compared to the sensitivity of the one-stage nozzle. Additionally, collection of particles in the range of 1–2.5 μm diameter using the multi-stage nozzle appears to provide better sensitivity compared to conventional collection methods, such as filtration, and aerosol spot collection through condensational growth. Gradually converging contractions provide a promising approach for obtaining spot samples for laser spectroscopic analysis and have the advantage of relatively higher flow throughputs that can be supported by small pumps suitable for portable instrumentation.

Declaration of competing interest

The authors declare that they have no competing financial interests.

Data availability

Data will be made available on request.

Acknowledgements

This research work was supported by a NIOSH intramural NORA grant. The authors would like to thank Dr. Lina Zheng for her suggestions for the successful processing of the experimental procedures. The authors would also like to thank Dr. Bon-Ki Ku, for his valuable advice and feedback on the manuscript.

Appendix A. Supplementary data

Supplementary data to this article can be found online at https://doi.org/10.1016/j.jaerosci.2023.106235.

References

Allen, M. D., & Raabe, O. G. (1982). Re-evaluation of millikan's oil drop data for the motion of small particles in air. *Journal of Aerosol Science, 13*(6), 537–547. https://doi.org/10.1016/0021-8502(82)90019-2

Barr, E. B., Hoover, M. D., Kanapilly, G. M., Yeh, H. C., & Rothenberg, S. J. (1983). Aerosol concentrator: Design, construction, calibration, and use. *Aerosol Science and Technology, 2*(4), 437–442. https://doi.org/10.1080/02786828308958647

Burwash, W., Finlay, W., & Matida, E. (2006). Deposition of particles by a confined impinging jet onto a flat surface at Re = 10 4. *Aerosol Science and Technology, 40*(3), 147–156. https://doi.org/10.1080/02786820500494551

Clift, R., Grace, J. R., & Weber, M. E. (1978). *Bubbles, drops and particles* (3rd ed.). Academic Press.

Dahneke, B., & Flachsbart, H. (1972). An aerosol beam spectrometer. *Journal of Aerosol Science, 3*(5), 345–349. https://doi.org/10.1016/0021-8502(72)90089-4

Davidson, C. I., Phalen, R. F., & Solomon, P. A. (2005). Airborne particulate matter and human health: A review. *Aerosol Science and Technology, 39*(8), 737–749. https://doi.org/10.1080/02786820500191348

Davies, C. N. (1945). Definitive equations for the fluid resistance of spheres. *Proceedings of the Physical Society, 57*(4), 259–270. https://doi.org/10.1088/0959-5309/57/4/301

Demokritou, P., Gupta, T., Ferguson, S., & Koutrakis, P. (2002). Development and laboratory characterization of a prototype coarse particle concentrator for inhalation toxicological studies. *Journal of Aerosol Science, 33*(8), 1111–1123. https://doi.org/10.1016/S0021-8502(02)00064-2

Diwakar, P. K., & Kulkarni, P. (2012). Measurement of elemental concentration of aerosols using spark emission spectroscopy. *Journal of Analytical Atomic Spectrometry, 27*(7), 1101–1109. https://doi.org/10.1039/c2ja30025g

Diwakar, P., Kulkarni, P., & Birch, M. E. (2012). New approach for near-real-time measurement of elemental composition of aerosol using laser-induced breakdown spectroscopy. *Aerosol Science and Technology, 46*(3), 316–332. https://doi.org/10.1080/02786826.2011.625059

Dockery, D. W., & Pope, C. A. (1994). Acute respiratory effects of particulate air pollution. *Annual Review of Public Health, 15*, 107–132. https://doi.org/10.1146/annurev.pu.15.050194.000543

Dowling, A. P. (2004). Development of nanotechnologies. *Materials Today, 7*(12 SUPPL), 30–35. https://doi.org/10.1016/S1369-7021(04)00628-5

Fallah, P., Hof, L. A., & Wuthrich, R. (2021). Fabrication of high-thickness and low surface roughness metal parts by a hybrid electrochemical manufacturing process. *Advances in Industrial and Manufacturing Engineering, 2*(May). https://doi.org/10.1016/j.aime.2021.100034

Fernández de la Mora, J., & Rosell-Llompart, J. (1989). Aerodynamic focusing of heavy molecules in seeded supersonic jets. *The Journal of Chemical Physics, 91*(4), 2603–2615. https://doi.org/10.1063/1.456969

Fredericks, S., & Saylor, J. R. (2018). Ring-shaped deposition patterns in small nozzle- to-Plate Distance impactors. *Aerosol Science and Technology, 52*(1), 30–37. https://doi.org/10.1080/02786826.2017.1377829

Hinds, W. C. (1999). *Aerosol technology: Properties, behavior, and measurement of airborne particles* (2nd ed.). New York: Wiley.

Hoek, G., M Krishnan, R., Beelen, R., Peters, A., Ostro, B., Brunekreef, B., & D Kaufman, J. (2013). Long-term air pollution exposure and cardio- respiratory mortality: A review. *Environmental Health, 12*(43). https://doi.org/10.1186/1476-069X-12-43

Keskinen, J., Janka, K., & Lehtimäki, M. (1987). Virtual impactor as an accessory to optical particle counters. *Aerosol Science and Technology, 6*(1), 79–83. https://doi.org/10.1080/02786828708959122

Kim, W.-G., Yook, S.-J., & Ahn, K.-H. (2013). Collection efficiency of rectangular slit-nozzle inertial impactors with impaction plates of elliptical concave curvature. *Aerosol Science and Technology, 47*(1), 99–105. https://doi.org/10.1080/02786826.2012.730162

Kim, M. M., & Zydney, A. L. (2004). Effect of electrostatic, hydrodynamic, and brownian forces on particle trajectories and sieving in normal flow filtration. *Journal of Colloid and Interface Science, 269*(2), 425–431. https://doi.org/10.1016/j.jcis.2003.08.004

Li, A., & Ahmadi, G. (1992). Dispersion and deposition of spherical particles from point sources in a turbulent channel flow. *Aerosol Science and Technology, 16*(4), 209–226. https://doi.org/10.1080/02786829208959550

Liu, P., Ziemann, P. J., Kittelson, D. B., & McMurry, P. H. (1995a). Generating particle beams of controlled dimensions and divergence: I. Theory of particle motion in aerodynamic lenses and nozzle expansions. *Aerosol Science and Technology, 22*(3), 293–313. https://doi.org/10.1080/02786829408959748

Liu, P., Ziemann, P. J., Kittelson, D. B., & McMurry, P. H. (1995b). Generating particle beams of controlled dimensions and divergence: II. Experimental evaluation of particle motion in aerodynamic lenses and nozzle expansions. *Aerosol Science and Technology, 22*(3), 314–324. https://doi.org/10.1080/02786829408959749

Marple, V. A., & Liu, B. Y. H. (1974). Characteristics of laminar jet impactors. *Environmental Science and Technology, 8*(7), 648–654. https://doi.org/10.1021/es60092a003

Maynard, A. D., & Kuempel, E. D. (2005). Airborne nanostructured particles and occupational health. *Journal of Nanoparticle Research, 7*(6), 587–614. https://doi.org/10.1007/s11051-005-6770-9

Mossman, B. T., & Churg, A. (1998). Mechanisms in the pathogenesis of asbestosis and silicosis. *American Journal of Respiratory and Critical Care Medicine, 157*(5 PART I), 1666–1680. https://doi.org/10.1164/ajrccm.157.5.9707141

Murphy, W. K., & Sears, G. W. (1964). Production of particulate beams. *Journal of Applied Physics, 35*(6), 1986–1987. https://doi.org/10.1063/1.1713788

Nemmar, A., Hoet, P. H. M., Vanquickenborne, B., Dinsdale, D., Thomeer, M., Hoylaerts, M. F., Vanbillioen, H., Mortelmans, L., & Nemery, B. (2002). Passage of inhaled particles into the blood circulation in humans. *Circulation, 105*(4), 411–414. http://circ.ahajournals.org/cgi/doi/10.1161/hc0402.104118.

Oberdörster, G. (2001). Pulmonary effects of inhaled ultrafine particles. *International Archives of Occupational and Environmental Health, 74*(1), 1–8. https://doi.org/10.1007/s004200000185

Pope, C. A., Burnett, R. T., Thurston, G. D., Thun, M. J., Calle, E. E., Krewski, D., & Godleski, J. J. (2004). Cardiovascular mortality and long-term exposure to particulate air pollution: Epidemiological evidence of general pathophysiological pathways of disease. *Circulation, 109*(1), 71–77.

Rao, N. P., Navascues, J., & Fernández de la Mora, J. (1993). Aerodynamic focusing of particles in viscous jets. *Journal of Aerosol Science, 24*(7), 879–892. https://doi.org/10.1016/0021-8502(93)90068-K

Schrader, B., Hoffmann, A., & Keller, S. (1991). Near-infrared fourier transform Raman spectroscopy: Facing absorption and background. *Spectrochimica Acta Part A: Molecular Spectroscopy, 47*(9–10), 1135–1148. https://doi.org/10.1016/0584-8539(91)80201-S

Sethi, V., & John, W. (1993). Particle impaction patterns from a circular jet. *Aerosol Science and Technology, 18*(1), 1–10. https://doi.org/10.1080/02786829308959580

Sioutas, C., Koutrakis, P., & Burton, R. M. (1994). Development of a low cutpoint slit virtual impactor for sampling ambient fine particles. *Journal of Aerosol Science, 25*(7), 1321–1330. https://doi.org/10.1016/0021-8502(94)90128-7

Sioutas, C., Koutrakis, P., & Olson, B. A. (1994). Development and evaluation of a low cutpoint virtual impactor. *Aerosol Science and Technology, 21*(3), 223–235. https://doi.org/10.1080/02786829408959711

Stacey, P., Hall, S., Stagg, S., Clegg, F., & Sammon, C. (2021). Raman spectroscopy and X-ray diffraction responses when measuring health-related micrometre and nanometre particle size fractions of crystalline quartz and the measurement of quartz in dust samples from the cutting and polishing of natural and artificial. *Journal of Raman Spectroscopy, 52*(6), 1095–1107. https://doi.org/10.1002/jrs.6110

Vidal-de-Miguel, G., & de la Mora, J. F. (2012). Continuously converging multistage focusing lenses to concentrate aerosols at high Reynolds numbers. *Aerosol Science and Technology, 46*(3), 287–296. https://doi.org/10.1080/02786826.2011.621906

Wei, S., Johnson, B., Breitenstein, M., Zheng, L., Snawder, J., & Kulkarni, P. (2022). Aerosol analysis using handheld Raman spectrometer: On-site quantification of trace crystalline silica in workplace atmospheres. *Annals of Work Exposures and Health, 66*(5), 656–670. https://doi.org/10.1093/annweh/wxab076

West, J. J., Cohen, A., Dentener, F., Brunekreef, B., Zhu, T., Armstrong, B., Bell, M. L., et al. (2016). What we breathe impacts our health: Improving understanding of the link between air pollution and health. *Environmental Science and Technology, 50*(10), 4895–4904. https://doi.org/10.1021/acs.est.5b03827

Zervaki, O., Stump, B., Keady, P., Dionysiou, D. D., & Kulkarni, P. (2023). NanoSpot^{TM} collector for aerosol sample collection for direct microscopy and spectroscopy analysis. *Aerosol Science and Technology, 57*(4), 342–354. https://doi.org/10.1080/02786826.2023.2167648

Zheng, L., Kulkarni, P., Birch, M. E., Deye, G., & Dionysiou, D. D. (2016). Near real-time measurement of carbonaceous aerosol using microplasma spectroscopy: Application to measurement of carbon nanomaterials. *Aerosol Science and Technology, 50*(11), 1155–1166. https://doi.org/10.1080/02786826.2016.1224804

Zheng, L., Kulkarni, P., Zavvos, K., Liang, H., Birch, M. E., & Dionysiou, D. D. (2017). Characterization of an aerosol microconcentrator for analysis using microscale optical spectroscopies. *Journal of Aerosol Science, 104*, 66–78. https://doi.org/10.1016/j.jaerosci.2016.11.007

Zhu, Z. W., Zhu, D., & Qu, N. S. (2008). Synthesis of smooth copper deposits by simultaneous electroforming and polishing process. *Materials Letters, 62*(8–9), 1283–1286. https://doi.org/10.1016/j.matlet.2007.08.031